ACS Sustainable Resource Management

pubs.acs.org/acssrm

Article

Enhancing Lithium Recycling Efficiency in Pyrometallurgical Processing through Thermodynamic-Based Optimization and Design of Spent Lithium-Ion Battery Slag Compositions

Haojie Li, Hao Qiu, Marko Ranneberg, Hugo Lucas, Torsten Graupner, Bernd Friedrich, Bengi Yagmurlu, Daniel Goldmann, Jens Bremer, and Michael Fischlschweiger*

Cite This: *ACS Sustainable Resour. Manage.* 2024, 1, 1170−1184

Read Online

ACCESS | Metrics & More | Article Recommendations | Supporting Information

ABSTRACT: The increasing demand for lithium in lithium-ion battery (LIB) applications necessitates innovative recycling strategies. Combined pyrometallurgical−hydrometallurgical recycling has gained increased attention for lithium recovery from slags. One challenge in the technological advancement of recycling lithium from spent LIBs with lithium-nickel-manganese-cobalt-oxide cathodes (NMC), characterized by a Li−Al−Si−Ca−Mn−O slag system, lies in the distribution of lithium across multiple silicate and oxide phases. Hence, the goal of this work is to significantly enrich the lithium in the single target phase γ-$LiAlO_2$ with thermodynamic-based optimization for tailored slag designs. This is achieved by coupling a sophisticated thermodynamic database and model reassessment related to practical NMC-type LIB slag system composition fields with Pareto optimization. Extensive experimental investigations are performed for model and design validations, and procedures for selecting the best phase candidates with individual lithium content are systematically presented. A strong nonlinear influence of CaO on the formation of the target product γ-$LiAlO_2$ could be revealed, where the addition of SiO_2 for lithium slagging needs to be limited to enrich lithium in the target phase. Higher amounts of added CaO and SiO_2, such as both at 30 wt %, result in the undesired transfer of lithium into other Li-containing phases. Based on this approach, an artificial slag is computationally designed for the first time, where theoretically 100% of the lithium is trapped in γ-$LiAlO_2$. After production of this slag and experimental analysis, it was found that 96% of lithium was transferred into γ-$LiAlO_2$. This demonstrates the great potential of thermodynamics-based artificial slag design for enhancing lithium recycling efficiency in LIB recycling processes.

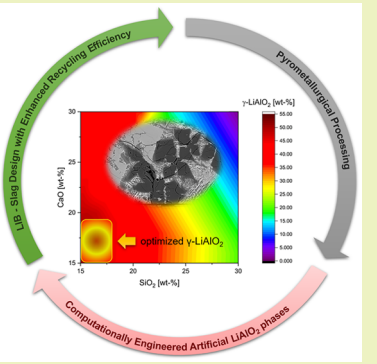

KEYWORDS: *engineering artificial minerals, Li-ion battery recycling, thermodynamic modeling, tailored solidification, high-temperature processing, Rietveld quantitative phase analysis, Pareto optimization*

1. INTRODUCTION

After the first commercialization of lithium-ion batteries (LIBs) in 1991,[1] they have attracted more and more attention in the field of energy markets such as for hybrid or electrical vehicles (EVs) or portable devices due to their high energy, power density, and lower self-discharge characteristics.[2−8] Consequently, the global market of LIBs is expected to reach $56 billion by 2024,[9] and the number of EVs on the roads is forecasted to be up to 253 million by 2030.[9] Obviously, with the strong growth of LIB utilization, there is a huge demand for critical raw materials such as cobalt, nickel, and lithium. However, natural resources for these metals are not evenly distributed and strictly regulated by specific countries.[8,10,11] More than 50% of cobalt ores is from the Democratic Republic of Congo, and about 80% of lithium is regulated by Australia and Chile.[8,11] The centralization of critical metal production in a few countries has raised concerns regarding supply chains and market prices.[12] The price of battery-grade lithium carbonate has increased by 5.6 times from 6500 dollars per metric ton in 2015 to 37,000 dollars per metric ton in 2022.[13] From 2018 to 2023, the consumption of lithium increased from 49,100 to 180,000 tons.[14] On the other hand, considering the average lifespan of LIBs being around 10 years,[15,16] it is anticipated that the volume of spent LIBs will exceed 5 million tons by 2030.[8,17] Hence, with the increasing amount of spent LIBs reaching their end of life (EOL), it is important to further develop energy-efficient recycling processes and techniques specifically tailored for the treatment of spent LIBs by considering a particularly high composition variability.

At present, there are four main strategies to recycle spent LIBs: biometallurgical,[18−21] hydrometallurgical,[22−26] direct

Received: February 20, 2024
Revised: May 10, 2024
Accepted: May 10, 2024
Published: May 18, 2024

recycling,[27−29] and pyrometallurgical.[24,30−34] The biometallurgical process enables the extraction of metals or metal compounds from spent LIBs with minimal environmental harm. Nevertheless, one drawback of this technique lies in the slow microbial cultivation and critical growth condition,[18] which currently restricts its application to the laboratory research stage. The hydrometallurgical process as one important recovery method uses acid or alkali leaching strategies for metals from spent LIBs into solution, followed by lithium extraction, selective precipitation, and conversion to get metal compounds.[8] In recent years, this route has gained increasing attention due to its advantages such as low energy consumption, high recovery rate, high purity of valuable metals,[8] and low Greenhouse Gas (GHG) emissions. However, there are challenges including the necessity of extensive presorting and pretreatment of the material,[8] the demand for significant quantities of reagents and water, and last but not least, the necessity for complex, expensive, and essential post-wastewater treatment.[35] Direct recycling is the process of removing cathode or anode material from an electrode for reconditioning and reuse in a remanufactured LIB.[27] This approach is gaining popularity, considering its comparative advantages in terms of lower energy and reagent costs compared with alternative processes. Moreover, it holds the potential to recover all components from LIBs and may retrieve the cathode material while preserving its intact crystal structure.[7] However, to achieve that, it is important that the spent LIBs are in good condition. Furthermore, additional steps such as presorting, dismantling, and employing diverse methods are necessary.[7] The pyrometallurgical route remains prevalent in industry based on its robustness and flexibility for treating various types of spent LIBs, where one major advantage of this method is the comparably small pretreatment or presorting, making it well-suited for handling different kinds of batteries and handling great LIB variability in their composition. As drawbacks, compared to other recycling strategies, higher energy consumption, costly waste gas treatment, and GHG emissions can be mentioned according to ref 36.

Currently, the combination of pyrometallurgical and hydrometallurgical routes has become attractive and shows several advantages.[37] One interesting process example is the Umicore process,[38] which combines spent-LIBs with slag builder and flux in a smelting furnace to enrich the cobalt, nickel, copper, and iron into alloy phases, followed by a hydrometallurgical refinement. The slag, which contains Li−Al−Si−Ca−Mn−O, is treated as construction material.[5] So far, the valuable significant lithium content in the slag, as reported in ref 38, ranges from 8 to 11 wt % and is not recycled due to the complexity of the multicomponent and multiphase behavior in the slag. Additionally, there is a heterogeneous distribution of lithium in various phases such as β-eucryptite, γ-$LiAlO_2$, Li_2MnSiO_4, and $LiAl_5O_8$. This complexity makes it quite challenging to recycle lithium effectively. The complex phase behavior of the slag can be influenced by the insertion of additional oxides. One example for a non-manganese-containing slag system, which was presented in our former study, indicated that the addition of flux, CaO and MgO, respectively, influences lithium enrichment in specific phases.[39,40] Additionally, the different valences of the manganese, resulting from different initial materials or synthesis routes, complicate slag phases due to the presence of various manganese-containing mineral phases. According to ref 41, when MnO_2 is selected as input material, the spinel phase forms under an air atmosphere and is described as $(Li_{(2x)}Mn^{2+}{}_{(1-x)})_{1+x}(Al_{(2-z)},Mn^{3+}{}_z)O_4$, where both Mn^{2+} and Mn^{3+} can coexist in the homogeneous solid solution. Furthermore, applying gel-combustion for synthesizing artificial minerals leads to the extra $LiMnO_2$ phase in the slag.[42]

This work was motivated to improve the lithium recovery efficiency of LIBs with lithium-nickel-manganese-cobalt-oxide cathodes (NMC). To achieve this goal, we develop and present a new approach for optimizing lithium enrichment due to artificial engineering phases during solidification for a manganese-containing slag system (Li−Al−Si−Ca−Mn−O system) within a particular and varying chemical composition field and based on thermodynamic modeling. Besides, this concept can also be applied to other battery types, which are characterized by this composition field. Hence, a thermodynamic-based slag and solidification model and optimization strategy is presented to transfer lithium effectively into the target phase lithium aluminate (γ-$LiAlO_2$). This tailored solid slag phase enables subsequent mechanical processing, flotation, and leaching processes, facilitating the effective recycling of lithium. The present study rests on a thermodynamic database and phase-specific models, developed within the framework of CALPHAD (Calculation of phase diagrams).[43,44] Subsequently, potentially formed phases within a specific compositional range practically relevant for the recycling of lithium-ion batteries (LIBs) are computed and presented. Furthermore, slag experiments are conducted, followed by chemical and mineralogical investigations to validate the model within the respective chemical composition field and provide the base for computational optimization of initial composition and certain solidification routes for the particular target phase. Results of this work include first the thermodynamic database and models, which are consequently validated by comparing them with experimental data. Second, the influence of initial composition and the addition of different quantities of flux, such as CaO and SiO_2, on the formation of the desired phase γ-$LiAlO_2$ is predicted. Third, Pareto optimization[45−47] is performed to design appropriate chemical compositions within the Li−Al−Si−Ca−Mn−O system, encompassing different phase fractions of Li_2O in the real industrial slag. This path aims to enhance lithium enrichment significantly in the target phase γ-$LiAlO_2$, as well as achieve a higher phase abundance of the desired phase while minimizing the quantity of the major raw material Li_2O and hence increasing recycling efficiency.

2. METHODS AND MATERIALS

2.1. Thermodynamic Database and Models. In this study, the Li−Al−Si−Ca−Mn-O system is expressed by the leading components Li_2O−Al_2O_3−SiO_2−CaO−MnO. The valence of manganese is exclusively considered as +2 due to the presence of graphite in the black mass or spent LIBs, which creates a strong reducing atmosphere in the pyrometallurgical route. Consequently, manganese oxidation and the influence of the partial pressure of oxygen are excluded within this study. With the development of CALPHAD databases over the past few decades, ten binary subsystems, Li_2O−Al_2O_3,[40,48] Li_2O−SiO_2,[40,49] Li_2O−CaO,[50] Li_2O−MnO,[51] Al_2O_3−SiO_2,[52] Al_2O_3−CaO,[52] Al_2O_3−MnO,[53] SiO_2−CaO,[54] SiO_2−MnO,[54] and CaO−MnO,[55] and seven ternary subsystems, Li_2O−CaO−Al_2O_3,[56] Li_2O−CaO−SiO_2,[40,56] Li_2O−Al_2O_3−SiO_2,[40,57] CaO−Al_2O_3−SiO_2,[52] Al_2O_3−SiO_2−MnO,[58] CaO−Al_2O_3−MnO,[59] and CaO−SiO_2−MnO,[59] have been critically assessed and optimized by the respective research groups. Despite these efforts, there remains a gap for the development of a comprehensive five-component thermodynamic database tailored

https://doi.org/10.1021/acssusresmgt.4c00064
ACS Sustainable Resour. Manage. 2024, 1, 1170−1184

Table 1. Overview of the Selected Stoichiometric Compounds and Liquid and Solid Solutions, Corresponding Thermodynamic Models, and Database of the $Li_2O-Al_2O_3-SiO_2-CaO-MnO$ System

Phase	Comments	Database
Li_2O	Stoichiometric compound	49
Al_2O_3, CaO, MnO, SiO_2, $Al_2Si_2O_7$, $MnSiO_3$, Mn_2SiO_4, $Mn_2Al_4Si_5O_{18}$, $Mn_3Al_2Si_3O_{12}$, $CaMnO_3$, Ca_2MnO_4, $CaMn_2O_4$, $Ca_3Mn_2O_7$, $CaMn_3O_6$, $Ca_2Mn_3O_8$, $Ca_4Mn_3O_{10}$, $CaMn_4O_8$, $CaMn_7O_{12}$, $Ca_3Al_2O_6$, $Ca_3Si_2O_7$, Ca_3SiO_5, $CaAl_2O_4$, $CaAl_2Si_2O_8$, $CaSiO_3$, Ca_2SiO_4, $CaAl_2Si_2O_8$	Stoichiometric compounds, the Gibbs energies of compounds were directly taken from the FT-Oxide database.	64
α-$LiAlO_2$	Stoichiometric compound, low-temperature polymorph	48
γ-$LiAlO_2$	Stoichiometric compound, high-temperature polymorph	48
Li_5AlO_4	Stoichiometric compound	40
$LiAl_5O_8$-LT	Stoichiometric compound, low-temperature polymorph	48
$LiAl_{11}O_{17}$	Stoichiometric compound	40
Li_4SiO_4	Stoichiometric compound	49
$Li_6Si_2O_7$	Stoichiometric compound	49
Li_8SiO_6	Stoichiometric compound	40
$Li_2Si_2O_5$-LT	Stoichiometric compound, low-temperature polymorph	49
$Li_2Si_2O_5$-HT	Stoichiometric compound, high-temperature polymorph	49
α-eucryptite, $LiAlSiO_4$-LT	Stoichiometric compound, low-temperature polymorph	57
β-eucryptite, $LiAlSiO_4$-HT	Stoichiometric compound, high-temperature polymorph	57
α-spodumene, $LiAlSi_2O_6$-LT	Stoichiometric compound, low-temperature polymorph	57
β-spodumene, $LiAlSi_2O_6$-HT	Stoichiometric compound, high-temperature polymorph	57
petalite, $LiAlSi_4O_{10}$	Stoichiometric compound	57
$Li_2Ca_3Si_6O_{16}$	Stoichiometric compound	56
liquid slag	Due to the short range ordering (SRO) in the liquid slag, the Gibbs energy of the liquid phase is calculated with MQM.[60−62] Besides Li^+, Mn^{2+}, Al^{3+}, Si^{4+}, and Ca^{2+}, the extra associate cation $LiAl^{4+}$ is introduced into this phase by considering the charge compensation effect.[65]	40, 51, 53−55, 58, 59
Li−Al rich spinel solid solution	Sublattice of this cubic Li−Al rich spinel can be described as $(Li^+, Al^{3+})^T [Li^+, Al^{3+}, Va]_2{}^O O_4$; the Gibbs energy of the spinel solid solution is described with CEF.[63]	40, 48
β-eucryptite solid solution, HT	Considering the SRO phenomenon in β-eucryptite solid solution, MQM[60−62] is applied for this solid solution. Besides, the excess solubility of SiO_2 is also considered in this model; the sublattice of β-eucryptite is assigned as $[LiAl^{4+}, VaSi^{4+}]SiO_4$.[57]	57
α-eucryptite solid solution, LT	There exists also excess solubility of SiO_2 in α-eucryptite. Thus, the sublattice of α-eucryptite is also expressed as $[LiAl^{4+}, VaSi^{4+}]SiO_4$ according to ref 57; considering different structures between α- and β-eucryptite, different Gibbs energies of the end-members are assigned.[57]	57
β-spodumene solid solution, HT	Excess solubility of SiO_2 in the β-spodumene is considered; the sublattice configuration is designed as $(LiAl^{4+}, VaSi^{4+})Si_2O_6$[57] and described with MQM.[60−62]	57
α-$LiAlO_2$ solid solution, LT	Low-temperature form. Due to the excess solubility of SiO_2, α-$LiAlO_2$ is extended as a solid solution. The sublattice structure of α-$LiAlO_2$ solid solution is expressed as $[LiAl^{4+}, VaSi^{4+}]O_2$;[57] two sublattice CEF[63] is used to describe the Gibbs energy of this solid solution.	57
γ-$LiAlO_2$ solid solution, HT	High-temperature form. Considering excess solubility of SiO_2. The sublattice structure of γ-$LiAlO_2$ solid solution is expressed as $[Li^+, Va]^{Li}[Al^{3+}, Si^{4+}]^M O_2$;[57] two sublattice CEF[63] describes the Gibbs energy of this solid solution.	40, 57
B-spinel $((Mn^{2+}, Al^{3+})[Mn^{2+}, Al^{3+}, Va]_2O_4)$, B-clinopyroxene $((Ca^{2+}, Mn^{2+})[Mn^{2+}]\{Si^{4+}\}SiO_6)$, A-wollastonite $((Ca^{2+}, Mn^{2+})SiO_3)$, a′$(Ca,Sr,Ba)_2SiO_4$ a-$(Ca,Sr)_2SiO_4$, A-melilite $((Ca^{2+})_2[Al^{3+}]\{Al^{3+}, Si^{4+}\}_2O_7)$, A-olivine $((Ca^{2+}, Mn^{2+})[Ca^{2+}, Mn^{2+}]SiO_4)$, mullite	Solid solutions, the Gibbs energies of phases were taken directly from the FT-Oxide database from FactSage.[64]	64

https://doi.org/10.1021/acssusresmgt.4c00064
ACS Sustainable Resour. Manage. 2024, 1, 1170−1184

Table 2. Crystal Structures Used for Rietveld Quantitative Phase Analysis

Phase	Crystal System	Space Group	Lattice Parameters	Reference
gehlenite ($Ca_2Al_2SiO_7$)	tetragonal	$P\bar{4}2_1m$	a = 7.685, c = 5.636	76
glaucochroite ($CaMnSiO_4$)	orthorhombic	$Pnma$	a = 4.913, b = 11.151, c = 6.488	71
β-eucryptite ($LiAlSiO_4$)	hexagonal	$P6_422$	a = 10.497, c = 11.200	69
γ-$LiAlO_2$	tetragonal	$P4_12_12$	a = 5.170, c = 6.295	70
Li_2MnSiO_4	monoclinic	$P2_1/c$	a = 6.337, b = 10.915, c = 5.073	72
			β = 90.987	
$LiAl_5O_8$	cubic	$P4_332$	a = 7.908	73
$Li_xMn_{1-2x}Al_{2+x}O_4$	cubic	$Fd\bar{3}m$	a = 7.990	this work

specifically for the slag system of LIBs and also for experimental validation. Furthermore, the phase behavior of this system and the validation of the thermodynamic database and models have not been addressed due to lack of systematic experimental study for the relevant chemical composition field in LIB pyrometallurgical recycling. The relevant subsystems as mentioned above are evaluated based on the experimental data in the literature. The corresponding model parameters, enthalpy, entropy, and Gibbs energies are listed in our previous work.[40,51] Theories about thermodynamic models such as Modified Quasichemical Model (MQM)[60−62] for liquid slags and Compound Energy Formalism (CEF)[63] for solid solutions can be found in the respective literature and are not explained again herein; rather, the reader is referred to the literature stated above. Stoichiometric compounds and liquid and solid solutions are selected based on the new experimental data established for the 5-component LIB slag system for the chemical composition field under investigation, and they are given in Table 1.

2.2. Slag Experiments. Artificial slags were made using commercial components with purities of ≥98% of Li_2CO_3, MnO, CaO (Sigma-Aldrich), Al_2O_3 (Nabalox), and SiO_2 (Sibelco's IOTA) as starting materials. The samples were sintered through a high-temperature furnace (Nabertherm HT 160/17) using ø65/55 × 130 mm isostatic graphite crucibles. In order to validate established thermodynamic models and databases, considering the real LIB slag from Umicore,[38] the chemical compositions of five samples are directly selected from previous work.[66] The heating strategy for producing the slag samples is given in the Supporting Information.

2.3. Chemical and Mineralogical Analysis. The mass fractions of Al_2O_3, SiO_2, CaO, and MnO were measured with a wavelength dispersive PANanlytical Axios XRF spectrometer at BGR on glass beads. Corrections for lithium contents in the samples were made using the Li data from ICP-MS. The matrix correction was performed using the method of De Jongh.[67] For the investigation, 1 g of the ground samples was first annealed at 750 °C to release volatile components and determine the loss on ignition. Then, the annealed samples were mixed with 5 g of lithium metaborate and melted in platinum crucibles at 1200 °C to form glass beads.

The lithium concentration was measured from diluted, acidified aqueous solutions by using a Thermo Fischer iCAP Triple Quadrupole ICP mass spectrometer. For this purpose, 50 mg of the ground samples was mixed with 0.5 mL of conc. HNO_3 as well as 4 mL of 48% HF and dissolved at 170 °C using a microwave digestion in pressure vessels. Afterwards, excess acids were removed at 90−120 °C. The residue was finally mixed with 5 mL of 6 M HCl, and the solution was diluted to 50 mL with double-distilled H_2O. For the calibration of the instrument, synthetic solutions with known concentrations were used. To control the results, a certified reference material (zinnwaldite: $KLiFe^{2+}Al(AlSi_3)O_{10}(F,OH)_2$) was analyzed in parallel.

Microstructure analyses were performed on polished, carbon coated samples embedded in epoxy resin using a MLA 650 F Quanta FEG scanning electron microscope (SEM; FEI Company) at BGR. The system is equipped with two energy-dispersive X-ray detectors (XFlash Detector 5030, Silicon Drift Detector; Bruker Nano) for semiquantitative element analysis.

The mineralogical composition of the slags was measured on powder samples using a PANalytical X'Pert Pro MPD X-ray diffractometer in reflection geometry at BGR with Co Kα radiation (40 kV and 40 mA), a variable divergence slit (20 mm irradiated length), primary and secondary soller slits (0.04 rad), antiscatter slits, a fixed incident beam mask (10 mm), a diffracted beam monochromator, and a point detector. The ground samples were transferred to the sample holder using the backloading method and measured in the angular range of 10−80° 2θ with a step size of 0.03° 2θ and a measurement time of 15 s per step. To determine the amorphous content, 20% corundum (Al_2O_3) was added to each sample as an internal standard. The identification of the slag phases was carried out with the program X'pert High Score Plus using the PDF-2 database from the International Center for Diffraction Data (ICDD). For the Rietveld refinement, the software Profex/BGMN[68] with the crystal structure data listed in Table 2 was utilized.

The slag phases with the general formula $Li_xMn_{1-2x}Al_{2+x}O_4$ ($0 \le x \le 0.5$) are $LiAl_5O_8$-rich solid solutions of the largely unknown solid solution series $MnAl_2O_4$−$LiAl_5O_8$ ($Li_{0.5}Al_{2.5}O_4$). The available data show that they crystallize in an inverse spinel structure with octahedrally coordinated Li, like the $LiAl_5O_8$-rich solid solutions of the solid solution series MAl_2O_4−$LiAl_5O_8$ (M = Zn, Mg) investigated by Rosciano et al.[74] or the $LiFe_5O_8$-rich solid solutions of the solid solution series $MnFe_2O_4$−$LiFe_5O_8$ studied by Wende,[75] and belong to the $Fd\bar{3}m$ space group.

Based on the slag experiments and corresponding experimental findings, the thermodynamic models and database are validated.

2.4. Pareto Optimization. In this study, further optimization of slag compositions is triggered by accounting for both the variation of Li_2O content and the loss of lithium through evaporation in the industrial slag production. To achieve this, the Pareto front methodology[45−47] is employed, using a search method applied to a large set of thermodynamic-based pre-evaluated simulation data. This approach facilitates the identification of trade-offs, considering three objectives with the following priorities: (1) to attain a greater enrichment of Li_2O in the desired phase, (2) to minimize the usage of the primary raw material Li_2O, and (3) to achieve a higher content of the γ-$LiAlO_2$ phase. The ranking of these data is carried out solely prior to achieving the complete binding of Li_2O within the target phase. Once the lithium content is sufficient for a 100% transfer to the target phase, only sample points with a transfer rate of 100% are chosen. At these points, the selection of optimal points is based on sorting for a lower Li_2O content while maximizing the phase amount of γ-$LiAlO_2$. The decision variables are the chemical composition of the flux and slag builder SiO_2 and CaO. Their content varies from 15 to 30 wt % in terms of total slag composition. The lower SiO_2 and CaO content is not considered, as insufficient flux and slag builder cannot effectively transfer lithium from spent LIBs or black mass into the slag phase.[38] Besides, the matrix composition in terms of Li_2O, Al_2O_3, and MnO is derived from the initial composition of sample A1 (see the Supporting Information). The mass fractions of Li_2O, Al_2O_3, and MnO remain constant at 16.2%, 74.3%, and 9.5%, respectively. Totally, 5738 raw data points are generated based on the validated thermodynamic model, predicting the quantity of the desired γ-$LiAlO_2$ phase across various chemical compositions. The range of these varied chemical compositions is presented in Table 3.

Thermodynamic prediction is based on two distinct cases. In the first case S1, any evaporation of lithium is excluded, whereas in the

https://doi.org/10.1021/acssusresmgt.4c00064
ACS Sustainable Resour. Manage. 2024, 1, 1170−1184

Table 3. Varied Chemical Composition in wt % Used for the Pareto Optimization for Two Different Cases

Case	Li_2O	Al_2O_3	SiO_2	CaO	MnO
S1	6.5−11.3	30.0−52.0	15.0−30.0	15.0−30.0	3.8−6.7
S2	5.2−9.1	29.7−52.0	15.0−30.0	15.0−30.0	5.1−8.9

second case S2, it is assumed that there is 20% of lithium loss via evaporation.

3. RESULTS AND DISCUSSIONS

The major findings on how lithium can be tailored in the target phase by applying the above described thermodynamic database, models, and Pareto optimization strategy are presented in this section. The XRD patterns of five samples (A1−A5) are presented in Figure 1. Their initial composition and the measured chemical composition after performing slag experiments are given in Table 4. Based on that, the lithium loss in the high-temperature slag experiments is confirmed. Second, in Figure 2, the measured solidified phase compositions are compared with the calculated equilibrium phase composition when the liquid phase just disappears. Specially, the predicted solidification sequence of the exemplified sample A3 is compared with chemical and mineralogical analysis. Then, the influence of the typical flux and slag builder CaO and SiO_2 on the formation of target phase γ-$LiAlO_2$ can be investigated and explained by the validated thermodynamic model. Finally, Pareto optimization is conducted to optimize the slag composition while accounting for variations in the Li_2O content in real industrial applications.

3.1. Lithium Evaporation in the High-Temperature Slag Experiments. With the procedure in ref 66, five samples were synthesized at 1450 °C under Ar atmosphere. In this case, the raw material Li_2CO_3 was decarbonated into Li_2O. A part of Li_2O was transferred into the flue gas at a high temperature, which affects the chemical composition of the samples investigated in solidification. To obtain the chemical composition of the samples after the high-temperature heating process, the chemical composition of the solidified samples was measured (Table 4). The measured phase compositions of samples A1−A5 are presented in Figure 1.

3.2. Experimental Validation of the Thermodynamic Model with the Specific Chemical Composition Field. The high-temperature thermal treatment leads to an evaporation of Li_2O, thereby inducing changes to the original weighted compositions compared to the solidification initial composition. To achieve accurate thermodynamic modeling of solidification, the measured chemical compositions of the A series samples are hence employed as inputs, enabling the calculation of the predicted solidified phases for each sample under equilibrium conditions. Since herein it is assumed that diffusion and reaction within the fully solid phases occur at a comparably slower rate, phase fractions are calculated at the liquid−solid transition, where the liquid phase is fully transformed. An additional remark can be made to the phase transition from α-$LiAlO_2$ to γ-$LiAlO_2$, which is according to refs 77 and 78 irreversible. Therefore, the different calculated

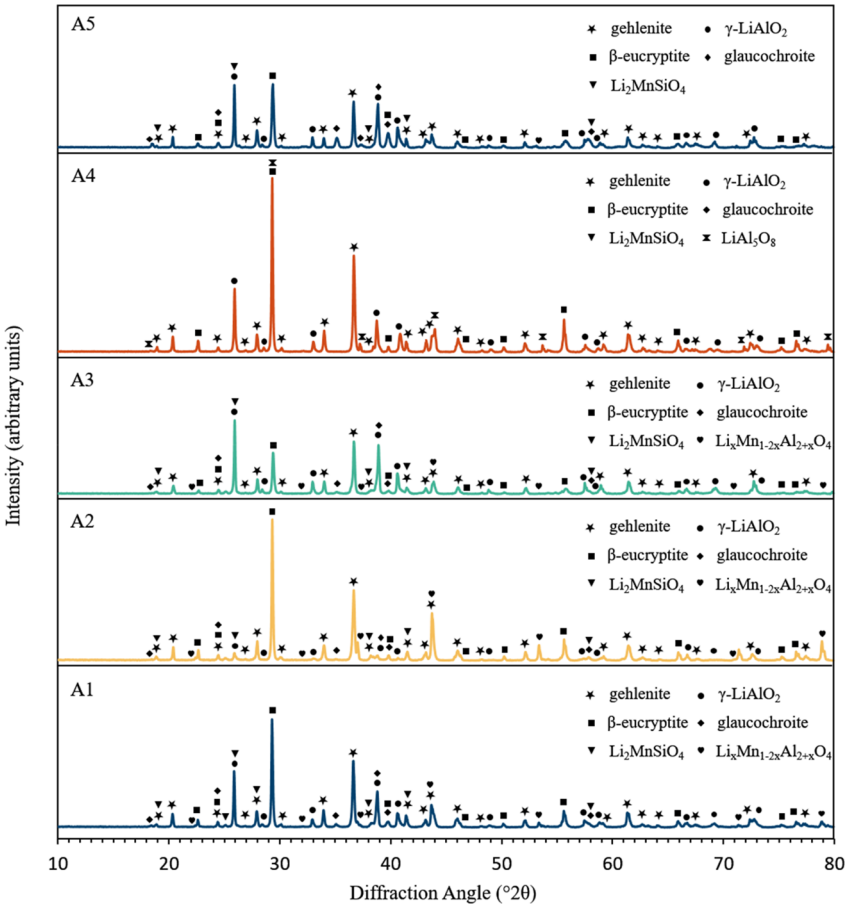

Figure 1. XRD patterns of samples A1−A5.

https://doi.org/10.1021/acssusresmgt.4c00064
ACS Sustainable Resour. Manage. 2024, 1, 1170−1184

Table 4. Weighed and Measured Chemical Composition of Slag Samples A1−A5 in wt % (Normalized to 100%)[a]

Sample	Li_2O	Al_2O_3	SiO_2	CaO	MnO
A1	8.9/8.0	41.0/41.2	27.4/27.9	17.4/17.8	5.3/5.1
A2	6.3/5.7	42.2/42.8	28.3/28.9	17.9/17.3	5.3/5.3
A3	11.6/10.6	39.7/40.1	26.5/27.0	16.9/16.8	5.3/5.5
A4	8.9/8.5	43.2/44.1	28.9/29.4	18.4/17.7	0.6/0.3
A5	8.9/8.7	38.7/38.9	25.8/26.2	16.5/16.2	10.1/10.0

[a]The contents of Al_2O_3, SiO_2, CaO, and MnO were measured by XRF and the Li_2O content was determined by ICP-MS.

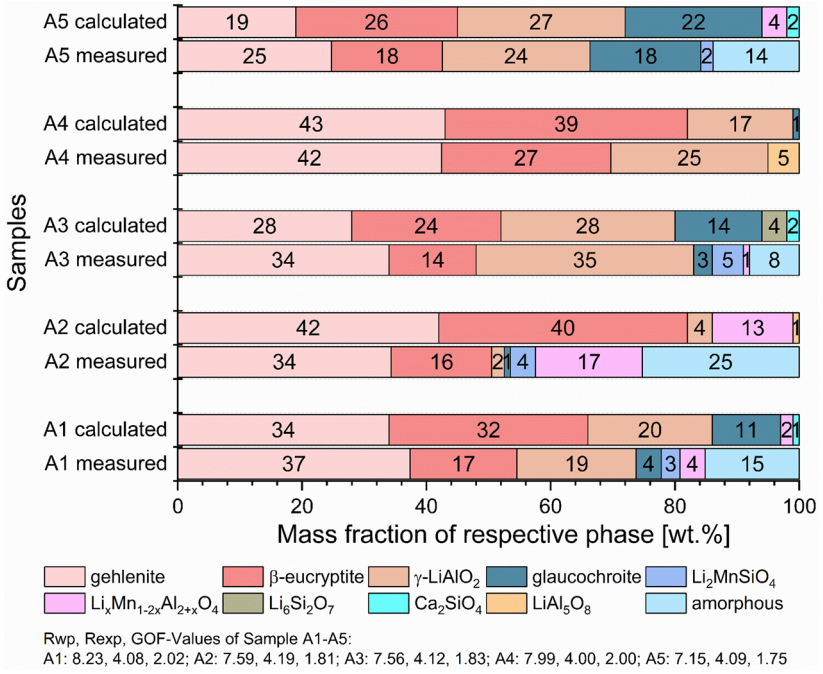

Figure 2. Comparison between the measured and calculated solidified phase composition under equilibrium conditions at 1 atm. The equilibrium phase composition is calculated when the liquid phase just disappears. The measured phase compositions are directly from ref 66.

polymorphs of $LiAlO_2$ are consistently considered as γ-$LiAlO_2$ in the present work. Besides, we assume that the eucryptite will maintain its high-temperature modification, i.e., β-eucryptite, during solidification at atmospheric pressure. For better comparison, the measured and calculated solidified phases of each sample are presented in Figure 2, in addition to the data given in Table S1.

Sample A1, positioned at the center of the sample composition matrix (Figure S2), contains 37 wt % gehlenite, indicating that it represents the most abundant solidified phase. In accordance with the current thermodynamic model calculations, the predicted phase amount for the gehlenite phase is 34 wt %, demonstrating a high level of agreement. Furthermore, the predicted phase amount for the key product γ-$LiAlO_2$ is 20 wt %, which closely aligns with the measured value of 19 wt %. The overestimation of the β-eucryptite phase, with a predicted phase amount of 32 wt % compared to the measured value of 17 wt %, is attributed to two factors. One reason for this overestimation is the absence of thermodynamic data for Li_2MnSiO_4 in the current thermodynamic modeling, which must be investigated in future studies. However, Li_2MnSiO_4 is present in minor quantities and often coexists with an amorphous phase, as depicted in Figure 3b for sample A3, indicating a non-equilibrium vs metastable state. Consequently, Li_2MnSiO_4 is disregarded and has not been investigated further in this study. By neglecting this phase, calculation leads to slight overestimation of β-eucryptite in the modeling. Furthermore, parts of Li_2O, SiO_2, and Al_2O_3 within the amorphous phase remain unconverted to β-eucryptite, resulting in a less measured β-eucryptite quantity than theoretical prediction owing to the occurrence of non-equilibrium conditions. These two factors also explain the reason the predicted phase amount of β-eucryptite is in all cases larger than experimental measurements. Sample A2, the sample with the lowest Li_2O content, results in the lowest measured content of the target product γ-$LiAlO_2$, quantified at 2 wt % based on experimental analysis, and a calculated phase composition of 4 wt %. Besides, the excess Al_2O_3 reacts in this sample with Li_2O and MnO to form a Li−Mn−Al spinel solid solution ($Li_xMn_{1-2x}Al_{2+x}O_4$), which has been determined as 17 wt % based on experimental measurements, with a slight deviation to the calculated amount of 13 wt %. Additionally, a frequent presence of amorphous phase has been identified in this sample. The larger discrepancy between the measured and calculated amounts of β-eucryptite is explained in analogy to the identical discrepancy in sample A1. Furthermore, both samples show similar gehlenite contents. As the amount of Li_2O increases, exemplified by sample A3, the phase composition of the target product γ-$LiAlO_2$ has reached its maximum value among the series of samples (measured: 35 wt %; model calculation: 28 wt %). In sample A4, the phase assemblage is relatively simple, comprising only four identified

https://doi.org/10.1021/acssusresmgt.4c00064
ACS Sustainable Resour. Manage. 2024, 1, 1170−1184

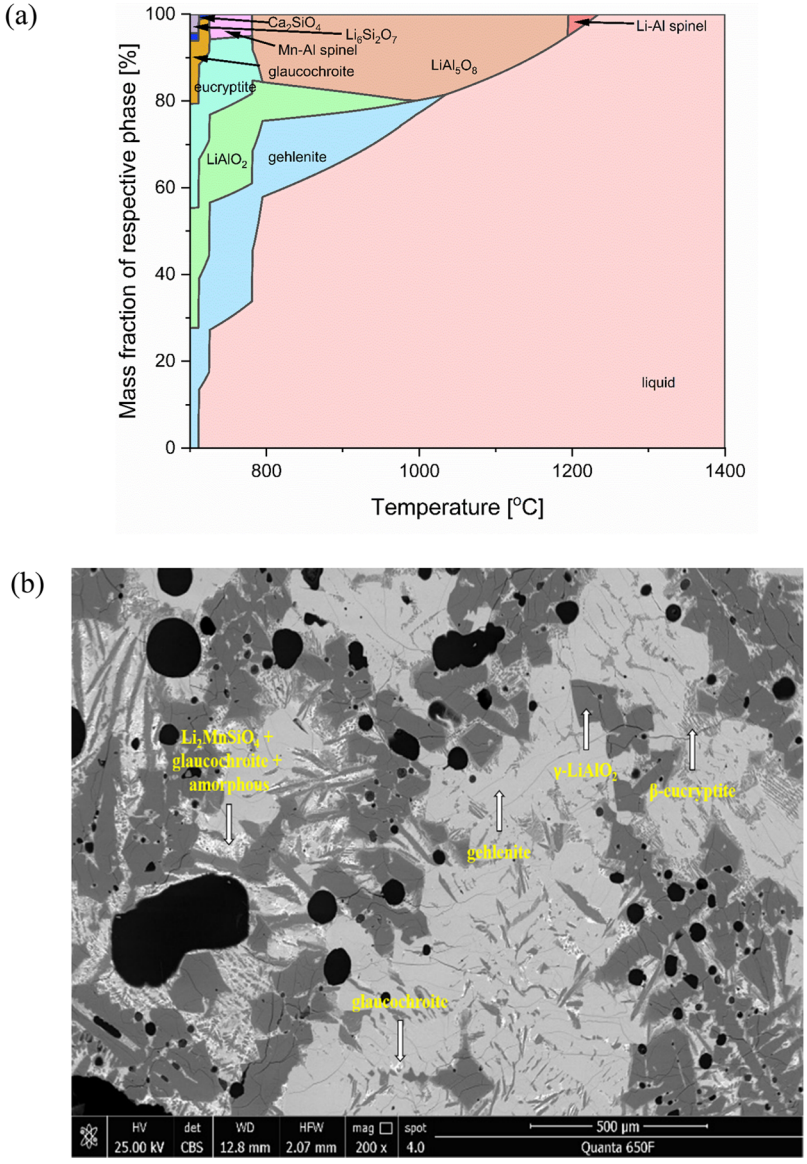

Figure 3. (a) Predicted equilibrium solidification process of sample A3 using the thermodynamic model and updated database. (b) Back scattered electron (BSE) image of solidified sample A3.

phases: gehlenite, β-eucryptite, γ-$LiAlO_2$, and $LiAl_5O_8$. Model calculations show a similar trend, with the phases in order of abundance being gehlenite, β-eucryptite, and γ-$LiAlO_2$. Although there should theoretically be traces of glaucochroite, their amounts are minimal and can be considered negligible. Moreover, the measured 5 wt % $LiAl_5O_8$ is not predicted. One possible explanation for this discrepancy is that the composition of sample A4 lies in the borderline composition region of $LiAl_5O_8$, which is not predicted by the model anymore. In sample A5, the predicted phase amount of γ-$LiAlO_2$ is 27 wt %, which closely aligns with the observed value of 24 wt %. Besides β-eucryptite and gehlenite, there exists a substantial quantity of glaucochroite, measured at 18 wt %. Remarkably, its predicted phase amount of 22 wt % also shows very good agreement with the measured value. It is evident that the dominant phases present in the samples are gehlenite, β-eucryptite, and γ-$LiAlO_2$. The model accurately predicts both the qualitative presence and quantitative contents of these phases. Notably, in the case of the target phase, γ-$LiAlO_2$, the maximal deviation between the predicted and measured amounts among all samples are 8 wt %. This shows that the model under the equilibrium assumptions has a high predictability of target phase γ-$LiAlO_2$ within the investigated chemical composition range of the manganese-containing slag system. It indicates that the phase formation of the γ-$LiAlO_2$ is mainly thermodynamically controlled. To improve the prediction accuracy of other mineral phases, their kinetic forces should be further investigated in future works.

Due to its highest content in the key product γ-$LiAlO_2$, sample A3 has been chosen for predicting its solidification process (Figure 3a). The obtained results from this prediction are then compared with the findings from the mineralogical investigation (Figure 3b), providing insights into the mechanism. In Figure 3a, a thermodynamic simulation illustrates the equilibrium solidification process initiated with a liquid slag composition corresponding to sample A3. At high temperatures (>1400−1234 °C), the slag remains in a liquid state. As the temperature decreases to 1234 °C, the Li−Al rich spinel, which is part of the $MnAl_2O_4$−$LiAl_5O_8$ spinel solid solution, starts to occur as the first precipitated crystalline

https://doi.org/10.1021/acssusresmgt.4c00064
ACS Sustainable Resour. Manage. 2024, 1, 1170−1184

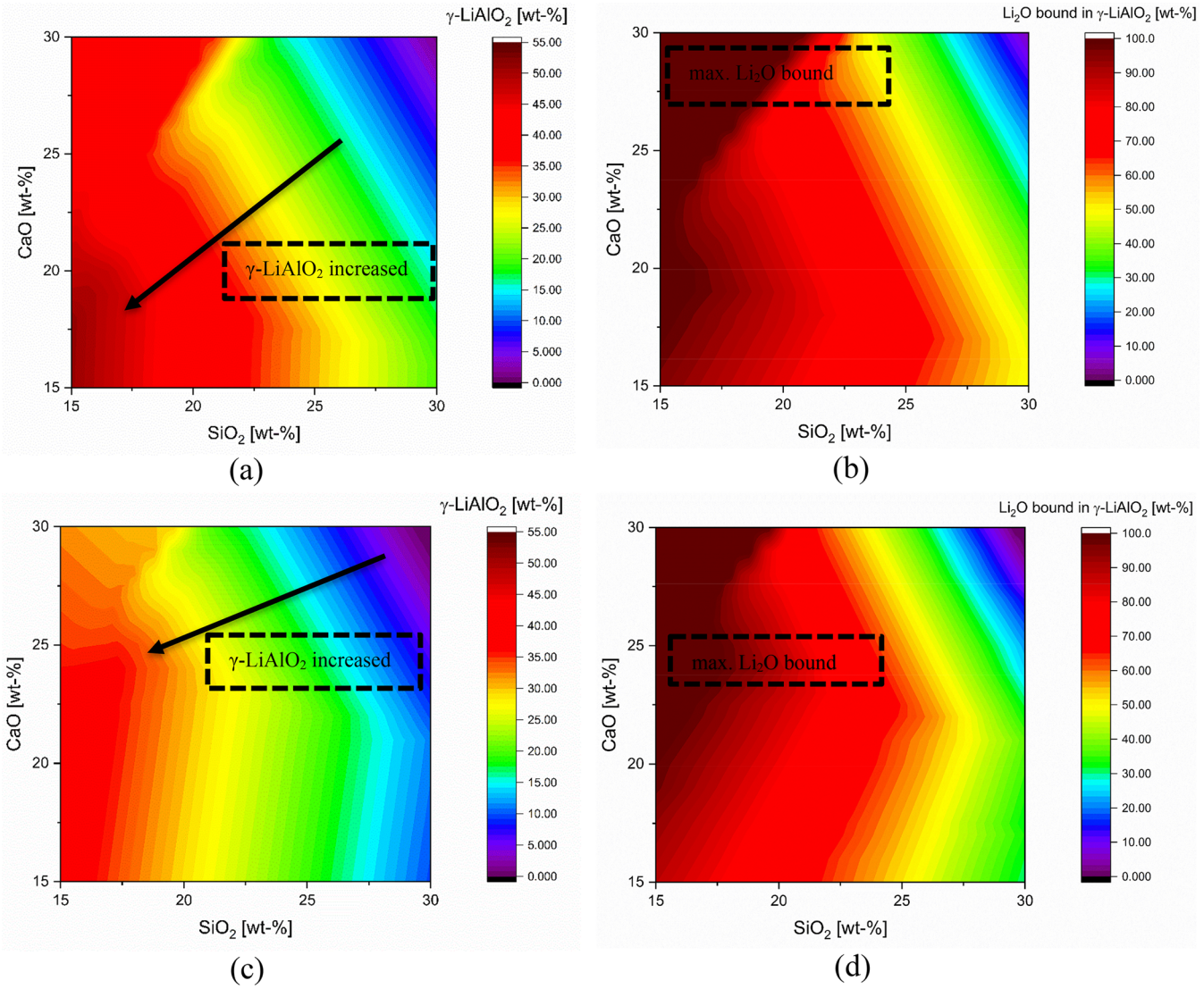

Figure 4. Predicted phase amount of γ-$LiAlO_2$ (a) and Li_2O bound in the target phase γ-$LiAlO_2$ (b) with varying additions of CaO and SiO_2 from 15 to 30 wt %, without considering lithium evaporation. Predicted phase amount of γ-$LiAlO_2$ (c) and Li_2O bound in the target phase γ-$LiAlO_2$ (d) with varying additions of CaO and SiO_2 from 15 to 30 wt %, under the assumption of 20% lithium evaporation.

phase. Then, it follows the formation of $LiAl_5O_8$. During the continuation of the cooling process, the predicted phase amount of $LiAl_5O_8$ gradually increases, reaching up to 19 wt %. However, at around 1030 °C, additional phases such as gehlenite and γ-$LiAlO_2$ start to appear, leading to a decrease in the predicted phase amount of $LiAl_5O_8$ while γ-$LiAlO_2$ and gehlenite continue to grow. As the temperature decreases to 794 °C, a new phase, β-eucryptite, is formed, followed by the formation of the manganese-containing phase, i.e., Mn−Al spinel, which is also part of the $MnAl_2O_4$−$LiAl_5O_8$ spinel solid solution. With the presence of the Mn−Al spinel, the former $LiAl_5O_8$ is completely transformed into other phases and disappears. This observation explains the absence of $LiAl_5O_8$ in solidified sample A3, as reported in the experimental measurements. Just before the liquid phase completely disappears, the second manganese-containing phase, glaucochroite, forms according to the solidification simulation. Furthermore, once the liquid phase completely disappears, another lithium-containing phase, $Li_6Si_2O_7$, should be present in a slight amount. Microstructure investigations by scanning electron microscopy (SEM) largely align with these results. They show that $MnAl_2O_4$−$LiAl_5O_8$ solid solutions ($Li_xMn_{1-2x}Al_{2+x}O_4$) crystallize first, followed by γ-$LiAlO_2$, gehlenite, and β-eucryptite. The close intergrowth of glaucochroite and Li_2MnSiO_4 with the amorphous components and their presence in the crystal interstices prove that these phases crystallize only afterwards, shortly before the residual melt solidifies glassy (Figure 3b).

3.3. Thermodynamic Model-Driven Slag Composition Design for Tailored γ-$LiAlO_2$ Formation. In the above section, the verification of the thermodynamic simulation with the updated database is achieved by comparing the experimental findings and theoretical model calculations concerning the solidified phases for different samples, where the specific solidification sequences are outlined for sample A3, which shows the largest amount of the target phase. In the above-mentioned samples, thermodynamic calculation reveals that the theoretical maximum phase amount of the desired product γ-$LiAlO_2$ in the sample A3 is limited to only 28 wt %. Additionally, this sample contains a significant proportion of another Li-containing phase, i.e., β-eucryptite, making up to 24 wt % of the composition. However, the distribution of lithium

https://doi.org/10.1021/acssusresmgt.4c00064
ACS Sustainable Resour. Manage. 2024, 1, 1170−1184

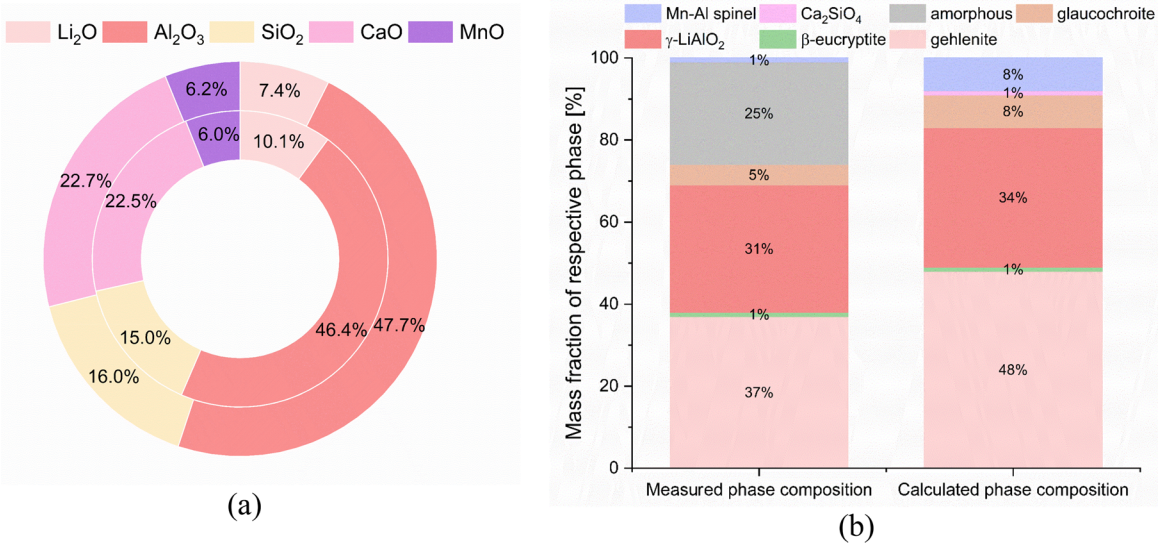

Figure 5. (a) Chemical composition of sample E1 in wt %; the inner ring represents the initial composition before the slag experiment, while the outer ring shows the measured chemical composition after the slag experiment. (b) Measured and calculated solidified phase composition of designed sample E1.

across different phases presents a challenge for downstream processes, especially froth flotation, as it aims to recapture lithium from γ-$LiAlO_2$. The distribution of lithium in multiple solidified slag phases hinders efficient extraction. In this section, we present the approach for optimizing the slag composition by using typical slag builders or fluxes, namely, SiO_2 and CaO. As it is shown in the section above, in addition to the target phase, other unwanted phases, i.e., lithium silicates, are produced. Therefore, it is aimed in this section to study the influence of SiO_2 and CaO in the context of reducing the lithium silicate content and increasing the target phase amount of γ-$LiAlO_2$. This enhances the recycling efficiency of the downstream process for lithium extraction from the target product γ-$LiAlO_2$. The matrix composition of the optimized samples is derived from the initial composition of the sample A1, with the following weight percentages: Li_2O, 16.2%; Al_2O_3, 74.3%; MnO, 9.5%; the content of CaO and SiO_2 is varied from 15 wt % to 30 wt % in terms of total slag composition. Additionally, the impact of lithium evaporation on the formation of the target product γ-$LiAlO_2$ is considered, and its influence on target phase formation is investigated. Therefore, two scenario calculations are carried out, in which results are presented in Figure 4. The first scenario calculations, shown in Figures 4a and 5b, do not consider any lithium losses, while the second scenario calculations, i.e., Figure 4c,d, takes a practically realistic lithium loss of 20% into account. From Sommerfeld et al.,[38] SiO_2 is crucially required as a suitable addition to promote the slagging of lithium, i.e., the transfer of lithium from spent LIBs or black mass into the slag. Nevertheless, the slagging of lithium does not promise that lithium is enriched in the single target phase γ-$LiAlO_2$. It can be diversely distributed into several lithium-containing mineral phases within the slag. For the investigated chemical composition field without considering lithium evaporation, Figure 4a shows that, to achieve a higher amount of target product γ-$LiAlO_2$, the addition of SiO_2 should be limited. As the SiO_2 content is increased up to 30 wt %, there will be a reduced amount of γ-$LiAlO_2$ present according to thermodynamic predictions. On the other hand, the influence of an addition of CaO on the target phase formation is nonlinear. Based on Figure 4a, when the SiO_2 content remains constant at 15 wt %, lower addition of CaO proves advantageous in obtaining a greater quantity of γ-$LiAlO_2$, with the maximum amount reaching up to 51 wt %.

However, in the higher SiO_2 composition range, the impact of CaO on the formation of the target phase is not always negative. For instance, the impact of increasing the CaO content from 15 to 22.5 wt % on γ-$LiAlO_2$ formation is not notably significant, when the total SiO_2 content is raised to the range of 20 to 22.5 wt %. However, with the same SiO_2 content, the phase fraction of γ-$LiAlO_2$ initially decreases to 20 wt % and then increases to the maximum of 36 wt % when the amount of CaO is further increased. In Figure 4b, the effect of the addition of CaO and SiO_2 on the enrichment of Li_2O within the single target product γ-$LiAlO_2$ is revealed. The highlight of simulation results, neglecting the lithium evaporation, shows that even a 100% Li_2O bound rate in γ-$LiAlO_2$ is theoretically achievable within the composition range of 15−21 wt % SiO_2 and 18−30 wt % CaO. In comparison to Figure 4a, one should note that the composition region with a higher phase amount of γ-$LiAlO_2$ is not identical with the region with higher lithium enrichment in the target phase. This phenomenon highlights the necessity of multi-objective optimization, which is explained in detail in the next section. In the pyrometallurgical recycling route, the evaporation of lithium during high-temperature processing is unavoidable. This leads to variation of the slag composition, resulting in a different impact of SiO_2 and CaO on the formation of γ-$LiAlO_2$ compared to previous simulation results. In Figure 4c, within the lower SiO_2 content range of 15 wt % to 17.5 wt %, the addition of CaO varying from 15 wt % to 25 wt % shows negligible influence on the formation of γ-$LiAlO_2$, and the average phase amount of γ-$LiAlO_2$ in this range is 36 wt % due to the lithium loss, which is significantly lower compared to the previous case. Additionally, when the continuous addition of CaO exceeds 25 wt %, it begins to impede the formation of γ-$LiAlO_2$. Furthermore, suitable amounts of CaO are beneficial for higher amounts of γ-$LiAlO_2$ once the content of SiO_2 has reached 30 wt %. In Figure 4c, thermodynamic simulation shows that 21 wt % of CaO can attain the highest amount of γ-

https://doi.org/10.1021/acssusresmgt.4c00064
ACS Sustainable Resour. Manage. 2024, 1, 1170−1184

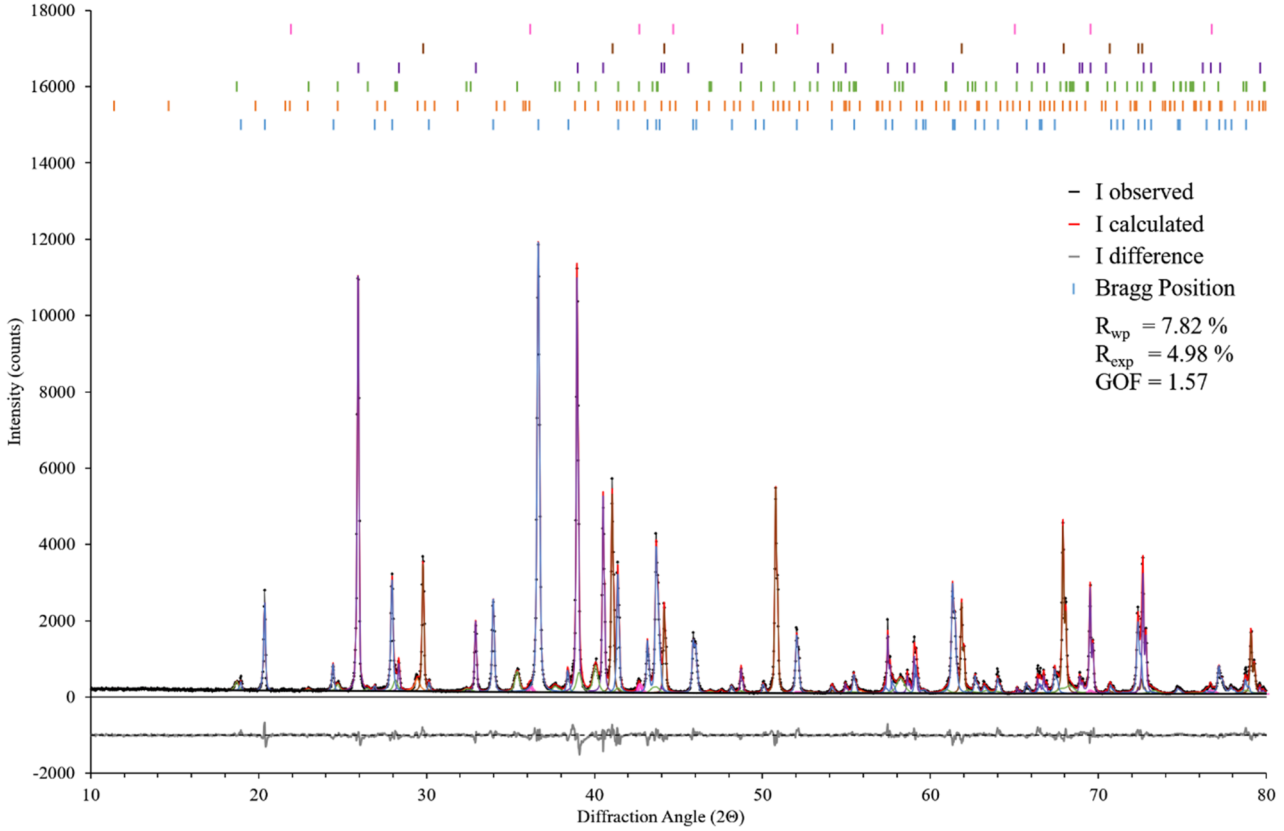

Figure 6. Rietveld refinement of sample E1.

$LiAlO_2$ when the SiO_2 content is 30 wt %. In Figure 4d, the region of higher lithium enrichment is more concentrated in the area of higher CaO addition. When 20% of Li_2O is volatilized, excess SiO_2 and Al_2O_3 require more CaO to react and form the gehlenite phase. In this case, lithium is less likely to form lithium silicate or β-eucryptite, thereby increasing the lithium enrichment in the target phase γ-$LiAlO_2$. Moreover, an excessive addition of SiO_2 negatively impacts the enrichment of lithium into the single phase γ-$LiAlO_2$ (i.e., approximately 30 wt % SiO_2); Li_2O cannot be effectively enriched into γ-$LiAlO_2$.

According to the thermodynamic simulation results presented above, a sample with an optimized composition was synthesized, which is denoted here as sample E1. This sample is designed with reduced SiO_2 content and moderate CaO content, comprising the following initial composition: Li_2O: 10.1 wt %; Al_2O_3: 46.4 wt %; SiO_2: 15.0 wt %; CaO: 22.5 wt %; MnO: 6.0 wt % (Figure 5). Sample E1 is prepared following the procedures outlined in the previous section on slag experiments. The objective behind its production is to verify the effectiveness of the thermodynamic model-driven slag composition design in achieving the desired γ-$LiAlO_2$ formation. It is essential to highlight that, during the slag experiments, there is lithium evaporation, which leads to changes in the actual chemical composition of the slag system. Therefore, the measured chemical composition of the slag will be utilized as input for conducting the thermodynamic simulations. After the slag production experiment, the chemical composition of solidified sample E1 is measured with Li_2O: 7.4 wt %; Al_2O_3: 47.7 wt %; SiO_2: 16.0 wt %; CaO: 22.7 wt %; MnO: 6.2 wt %. Approximately 27% of the total lithium content evaporates at elevated temperatures. This measured composition is utilized as input data to predict the solidified phases. In the designed sample E1, thermodynamic simulations indicate that, upon the complete disappearance of the liquid phase, the prominent solidified phases are predicted to consist of 48 wt % gehlenite, 34 wt % γ-$LiAlO_2$, 8 wt % glaucochroite, and 8 wt % Mn−Al spinel.

Besides, in this sample, lithium can theoretically achieve almost 100% enrichment in the desired phase γ-$LiAlO_2$ under the thermodynamic equilibrium condition. Figure 6 shows the Rietveld refinement of slag sample E1. The figures of merit (R_{wp}, R_{exp}, and GOF) and the difference plot indicate a good agreement between observed and calculated intensity values.

Based on the experimental results, the prominent predicted phases are identified as 37 wt % gehlenite, 31 wt % γ-$LiAlO_2$, and 5 wt % glaucochroite, apart from the amorphous phase. Additionally, there is another lithium-containing phase, namely, β-eucryptite. However, the measured quantity of β-eucryptite is negligible, accounting for only 1 wt %. Significantly, mineralogical measurements reveal that 2% of the lithium present in solidified sample E1 is identified within the amorphous phase. This observation suggests that, apart from the 2% of lithium that is bound within the β-eucryptite, a notable 96% of the lithium in the solidified sample has effectively transitioned into the desired phase, γ-$LiAlO_2$. Furthermore, the production of the amorphous phase is diminished by reducing the cooling rate during the solidification process, and an increased transfer of lithium into the target phase can be expected.

3.4. Pareto Optimization for Enhancing Lithium Recycling Efficiency. With the updated thermodynamic prediction and experimental measurements, sample E1 turned out to be a viable candidate for upscaling, attributed not only

https://doi.org/10.1021/acssusresmgt.4c00064
ACS Sustainable Resour. Manage. 2024, 1, 1170−1184

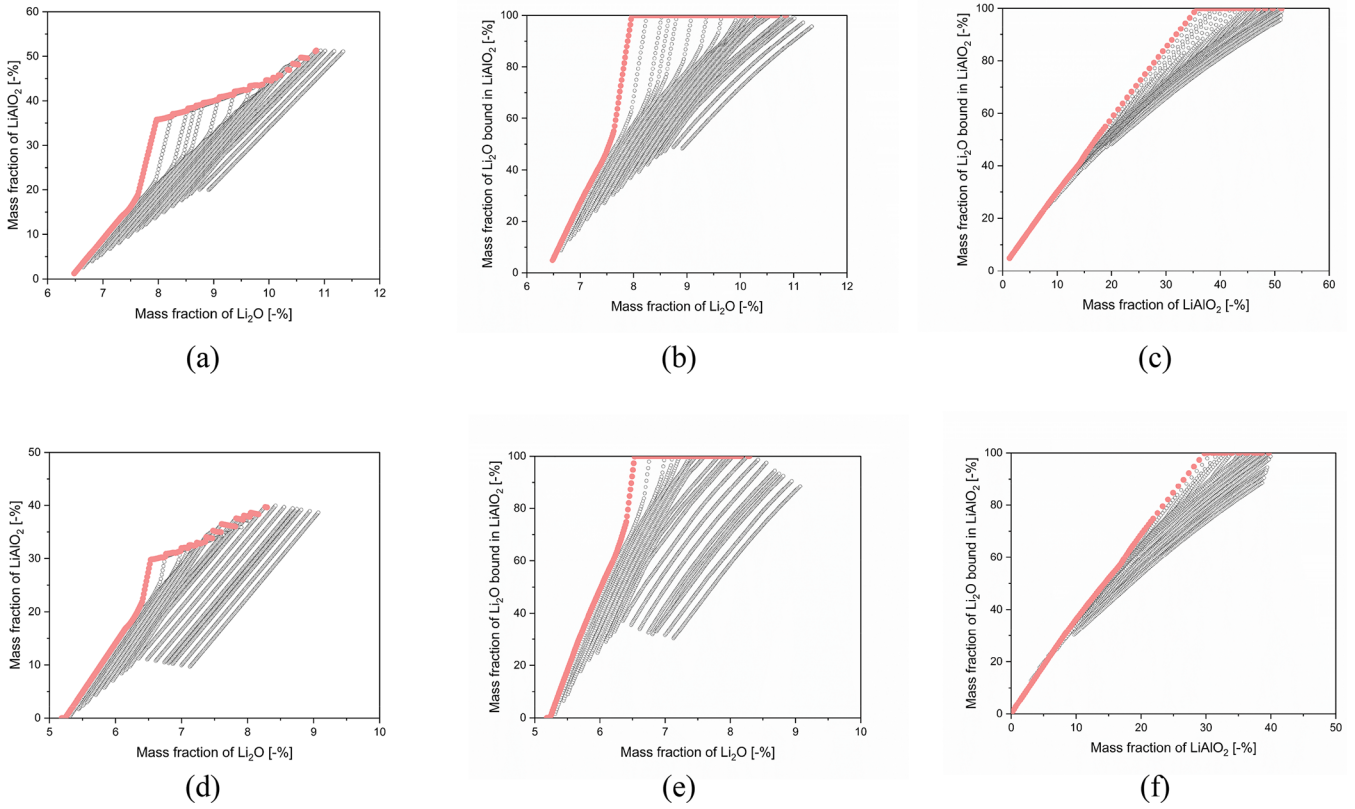

Figure 7. Calculated Pareto front depicting prioritized objectives: (1) maximized mass fraction of Li_2O bound in γ-$LiAlO_2$, (2) minimized mass fraction of Li_2O, and (3) maximized mass fraction of γ-$LiAlO_2$. Results are presented for two scenarios: (a–c) show results without lithium loss consideration, while (d–f) consider 20% lithium loss assumption. Raw data points are denoted in black, while the pink points denote the Pareto front set.

to its higher γ-$LiAlO_2$ phase fraction but also to its enhanced rate of lithium binding within this specific target phase. Nevertheless, in practical industrial applications, when feeding diverse types of spent LIBs or black mass, the corresponding lithium content varies, thereby influencing the total lithium content in the slag phase. In most cases, achieving a weight fraction of Li_2O equivalent to the optimized sample E1 is a challenging issue. Therefore, the utilization of Pareto optimization,[45−47] a typical technique employed for addressing multi-objective optimization problems, is implemented to formulate a slag composition in the presence of variations in the quantities of Li_2O. The input dataset originates from Figure 4, wherein the matrix composition denoted by Li_2O, Al_2O_3, and MnO corresponds to 16.2%, 74.3%, and 9.5%, respectively. The objective is to identify trade-offs, specifically Pareto front points, to maximize lithium enrichment in the target phase while minimizing the consumption of the primary raw material Li_2O in two different cases. In the current investigation, our focus is directed toward assigning a higher priority to the enhanced enrichment of Li_2O within the target phase. Subsequently, we emphasize the reduction in the addition of Li_2O, while aiming to achieve a greater quantity of the γ-$LiAlO_2$ phase.

In Figure 7a,b, mass fraction of Li_2O is varied from 6.5 wt % to 11.3 wt % due to the addition of different amounts of SiO_2 and CaO. However, the optimized points are only occurring in the range of 6.5 wt % to 10.9 wt % Li_2O. Excessive additions of Li_2O above 10.9 wt % are undesirable due to the formation of other lithium-containing phases. The highest phase quantity of γ-$LiAlO_2$ within the Pareto front depicted in Figure 7a can be reached at 51.3 wt %. In this case, the Li_2O content is 10.9 wt %. It is worth noting that some points, which contain a higher amount of the target phase, are not selected as optimized points. For instance, at 10.3 wt % Li_2O, the point chosen as optimized contains 47.0 wt % γ-$LiAlO_2$, disregarding the higher 47.8 wt % counterpart. This discrepancy arises from variable Li_2O enrichment in γ-$LiAlO_2$. Although equal amounts of Li_2O are added, varying amounts of other raw materials (e.g., SiO_2) can dissolve into γ-$LiAlO_2$, thereby increasing the mass fraction of γ-$LiAlO_2$. This situation may lead to the excretion of lithium from γ-$LiAlO_2$, resulting in the formation of another lithium-containing phase. As a result, Li_2O enrichment in the target phase is reduced. Moreover, Figure 7a,b reveals optimal points with noticeable gaps, exemplified by the range 10.2−10.3 wt % Li_2O. This gap stems from enriching Li_2O in the target phase. Figure 7b also show that, once the Li_2O content is more than 8.0 wt %, Li_2O can be fully transferred into the target phase with varied addition of the other oxides. However, at some certain Li_2O contents, complete enrichment into γ-$LiAlO_2$ cannot be achieved. These data points are purposefully excluded during the Pareto optimization process. The presence of these gaps can be ascribed to the intrinsic limitations of numerical methodologies, wherein achieving a complete 100% transfer rate of Li_2O into the target phase at some certain initial compositions remains unfeasible. Furthermore, in Figure 7c, the interrelation between the Li_2O enrichment in the target phase and phase amount of γ-$LiAlO_2$ is shown. Even with the same phase amount of γ-$LiAlO_2$, the Li_2O enrichments are different under the different chemical compositions of the samples. When the mass fraction of γ-$LiAlO_2$ is around 35.8%,

https://doi.org/10.1021/acssusresmgt.4c00064
ACS Sustainable Resour. Manage. 2024, 1, 1170−1184

the Li_2O enrichment in the target phase γ-$LiAlO_2$ ranges between 74.8% and 100%. This is due to the presence of varying amounts of other oxides such as CaO, SiO_2, and MnO, which can influence the formation of γ-$LiAlO_2$ as well as other lithium-containing phases, such as β-eucryptite and the Li−Al spinel. Therefore, Pareto optimization has been performed to identify the optimal slag composition that allows for the maximum binding of lithium to γ-$LiAlO_2$, while also generating a considerable amount of γ-$LiAlO_2$ which could be efficiently separated in the downstream processing for recycling. In the second case S2, assuming 20% Li_2O evaporation, the optimized range of Li_2O content in Figure 7d,e becomes narrower and shifts to 5.2−8.3 wt %, and the predicted mass fraction of γ-$LiAlO_2$ in Figure 7d,f is significantly decreased compared to that in Figure 7a,c. Furthermore, in Figure 7f, the required minimal amount of Li_2O content to achieve a 100% binding rate of lithium to γ-$LiAlO_2$ is decreased to 6.5 wt %, compared to 8.0 wt % in Figure 7b. This is attributed to the loss of 20% Li_2O, altering the chemical composition of the sample and making the previously optimal points unsuitable for this situation. Therefore, due to the high sensitivity of this slag system, an accurate thermodynamic database and models are essential for understanding the interrelation between the input materials and the target phase. This understanding serves as the basis for further Pareto optimization.

4. CONCLUSIONS

Due to its robustness, the combined pyrometallurgical−hydrometallurgical process route is gaining more and more attention for the recycling of LIBs, especially on a large scale and dealing with LIB composition variations. A significant hurdle in the technological advancement of recycling lithium from spent LIBs via slag, which consists of a Li−Al−Si−Ca−Mn−O system, is the distribution of lithium into multiple Li-containing silicate and oxide phases. This complexity presents a barrier to downstream processing. To increase lithium recycling efficiency, one of the major tasks is to enrich lithium in a single target phase, i.e., γ-$LiAlO_2$. In the present study, sophisticated thermodynamic databases and models in terms of this slag system are evaluated and combined based on the previous literature within the CALPHAD framework in a certain practically relevant chemical composition field. Extensive experimental investigations have been performed such that the model predictions could be validated. With respect to the target phase, the root-mean-square deviation is 5%. With the thermodynamic model, the influence of CaO on the formation of γ-$LiAlO_2$ as well as lithium enrichment is studied, and a strong nonlinear relationship turned out. The addition of SiO_2 after a certain limit shows a decreasing behavior of the target phase. Higher amounts of added CaO and SiO_2, both at 30 wt %, lead to unwanted distribution of lithium in other Li-containing phases. Based on the validated thermodynamic model, an artificial slag composition is computed for the first time, where 100% of the lithium is trapped in γ-$LiAlO_2$, by optimizing flux amounts. The computational composition design of the slag was used to experimentally generate such a slag, and it is gained by experimental analysis that 96% of the Li is trapped in γ-$LiAlO_2$. This emphasizes the strength of thermodynamic-based slag design for enhancing LIB recycling efficiency in pyrometallurgical processing routes. Additionally, it is revealed that regions of higher concentrations of the target phase γ-$LiAlO_2$ do not coincide with the regions of higher Li_2O bound in γ-$LiAlO_2$. This shows how optimizations can be used to identify trade-offs between achieving higher lithium enrichment in the target phase and minimizing the addition of the major raw material Li_2O, where at the same time the amount of the target phase is maximized.

■ ASSOCIATED CONTENT

Supporting Information

The Supporting Information is available free of charge at https://pubs.acs.org/doi/10.1021/acssusresmgt.4c00064.

Heating strategy for producing the slag samples; sample composition matrix; comparison between the measured (m) and calculated (c) solidified phase composition of samples A1−A5 (PDF)

■ AUTHOR INFORMATION

Corresponding Author

Michael Fischlschweiger − *Chair of Technical Thermodynamics and Energy Efficient Material Treatment, Institute of Energy Process Engineering and Fuel Technology, Clausthal University of Technology, 38678 Clausthal-Zellerfeld, Germany;* orcid.org/0000-0002-0064-1292; Email: michael.fischlschweiger@tu-clausthal.de

Authors

Haojie Li − *Chair of Technical Thermodynamics and Energy Efficient Material Treatment, Institute of Energy Process Engineering and Fuel Technology, Clausthal University of Technology, 38678 Clausthal-Zellerfeld, Germany*

Hao Qiu − *Department of Mineral and Waste Processing, Institute of Mineral and Waste Processing, Clausthal University of Technology, 38678 Clausthal-Zellerfeld, Germany*

Marko Ranneberg − *Federal Institute for Geosciences and Natural Resources (BGR), 30655 Hannover, Germany*

Hugo Lucas − *Institute of Process Metallurgy and Metal Recycling (IME), RWTH Aachen University, 52056 Aachen, Germany*

Torsten Graupner − *Federal Institute for Geosciences and Natural Resources (BGR), 30655 Hannover, Germany*

Bernd Friedrich − *Institute of Process Metallurgy and Metal Recycling (IME), RWTH Aachen University, 52056 Aachen, Germany*

Bengi Yagmurlu − *Department of Mineral and Waste Processing, Institute of Mineral and Waste Processing, Clausthal University of Technology, 38678 Clausthal-Zellerfeld, Germany;* orcid.org/0000-0002-5376-1677

Daniel Goldmann − *Department of Mineral and Waste Processing, Institute of Mineral and Waste Processing, Clausthal University of Technology, 38678 Clausthal-Zellerfeld, Germany*

Jens Bremer − *Institute of Chemical and Electrochemical Process Engineering, Clausthal University of Technology, 38678 Clausthal-Zellerfeld, Germany*

Complete contact information is available at: https://pubs.acs.org/10.1021/acssusresmgt.4c00064

Notes

The authors declare no competing financial interest.

■ ACKNOWLEDGMENTS

The project on which this publication is based was funded by the German Federal Ministry of Education and Research within the Competence Cluster Recycling & Green Battery (greenBatt) under the grant number 03XP0336A. The authors are responsible for the content of this publication.

■ REFERENCES

(1) Bae, H.; Kim, Y. Technologies of lithium recycling from waste lithium ion batteries: a review. *Materials Advances* **2021**, *2*, 3234−3250.
(2) Zhu, P.; Gastol, D.; Marshall, J.; Sommerville, R.; Goodship, V.; Kendrick, E. A review of current collectors for lithium-ion batteries. *J. Power Sources* **2021**, *485*, No. 229321.
(3) Goodenough, J. B.; Kim, Y. Challenges for rechargeable Li batteries. *Chem. Mater.* **2010**, *22* (3), 587−603.
(4) Hou, C.; Yang, W.; Xie, X.; Sun, X.; Wang, J.; Naik, N.; Pan, D.; Mai, X.; Guo, Z.; Dang, F.; Du, W. Agaric-like anodes of porous carbon decorated with MoO_2 nanoparticles for stable ultralong cycling lifespan and high-rate lithium/sodium storage. *J. Colloid Interface Sci.* **2021**, *596*, 396−407.
(5) Mohr, M.; Weil, M.; Peters, J.; Wang, Z. Recycling of Lithium-Ion Batteries. *Encyclopedia of Electrochemistry* **2020**, 1.
(6) Duan, X.; Zhu, W.; Ruan, Z.; Xie, M.; Chen, J.; Ren, X. Recycling of Lithium Batteries-A Review. *Energies* **2022**, *15*, 1611.
(7) Baum, Z. J.; Bird, R. E.; Yu, X.; Ma, J. Lithium-Ion Battery Recycling Overview of Techniques and Trends. *ACS Energy Lett.* **2022**, *7* (2), 712−719.
(8) Yu, X.; Li, W.; Gupta, V.; Gao, H.; Tran, D.; Sarwar, S.; Chen, Z. Current Challenges in Efficient Lithium-Ion Batteries' Recycling: A Perspective. *Global Challenges* **2022**, *6* (12), No. 2200099.
(9) Fan, E.; Li, L.; Wang, Z.; Lin, J.; Huang, Y.; Yao, Y.; Chen, R.; Wu, F. Sustainable Recycling Technology for Li-Ion Batteries and Beyond: Challenges and Future Prospects. *Chem. Rev.* **2020**, *120* (14), 7020−7063.
(10) Dehaine, Q.; Tijsseling, L. T.; Glass, H. J.; Törmänen, T.; Butcher, A. R. Geometallurgy of cobalt ores: A review. *Minerals Engineering* **2021**, *160*, No. 106656.
(11) Zeng, A.; Chen, W.; Rasmussen, K. D.; Zhu, X.; Lundhaug, M.; Muller, D. B.; Tan, J.; Keiding, J. K.; Liu, L.; Dai, T.; Wang, A.; Liu, G. Battery technology and recycling alone will not save the electric mobility transition from future cobalt shortages. *Nat. Commun.* **2022**, *13*, 1341.
(12) Schmidt, M. *Rohrstoffrisikobewertung-Lithium*; DERA-Rohrstoffinformationen, 2023; https://www.deutsche-rohstoffagentur.de/DE/Gemeinsames/Produkte/Downloads/DERA_Rohstoffinformationen/rohstoffinformationen-54.pdf;jsessionid=DE70934E86142D96C3500CEDE3CB5AEE.internet991?__blob=publicationFile&v=4.
(13) Garside, M. *Average lithium carbonate price from 2010 to 2022 (in U.S. dollars per metric ton)*; 2023; https://www.statista.com/statistics/606350/battery-grade-lithium-carbonate-price/ (accessed on 2023-06-17).
(14) U. S. Geological Survey *Mineral Commodity Summaries*; January 2024.
(15) Chen, M.; Ma, X.; Chen, B.; Arsenault, R.; Karlson, P.; Simon, N.; Wang, Y. Recycling End-of-life Electric Vehicle Lithium-Ion Batteries. *Joule* **2019**, *3* (11), 2622−2646.
(16) Xu, P.; Dai, Q.; Gao, H.; Liu, H.; Zhang, M.; Li, M.; Chen, Y.; An, K.; Meng, Y.; Liu, P.; Li, Y.; Spangenberger, J. S.; Gaines, L.; Lu, J.; Chen, Z. Efficient Direct Recycling of Lithium-Ion Battery Cathodes by Targeted Healing. *Joule* **2020**, *4* (12), 2609−2626.
(17) KPMG. *Lithium-Ion Battery Sector: Developing a Promising Sector for Quebec's Economy*; Propulsion Quebec: Montreal, QC, 2019.
(18) Zhou, M.; Li, B.; Li, J.; Xu, Z. Pyrometallurgical Technology in the Recycling of a Spent Lithium Ion Battery: Evolution and the Challenge. *ACS ES&T Engineering* **2021**, *1* (10), 1369−1382.
(19) Horeh, N. B.; Mousavi, S.; Shojaosadati, S. Bioleaching of valuable metals from spent lithium-ion mobile phone batteries using Aspergillus niger. *J. Power Sources* **2016**, *320*, 257−266.
(20) Xin, B.; Zhang, D.; Zhang, X.; Xia, Y.; Wu, F.; Chen, S.; Li, L. Bioleaching mechanism of Co and Li from spent lithium-ion battery by the mixed culture of acidophilic sulfur-oxidizing and iron-oxidizing bacteria. *Bioresource Technology* **2009**, *100* (24), 6163−6169.
(21) Mishra, D.; Kim, D. J.; Ralph, D.; Ahn, J. -G; Rhee, Y.-H. Bioleaching of metals from spent lithium ion secondary batteries using Acidithiobacillus ferrooxidans. *Waste management* **2008**, *28* (2), 333−338.
(22) Gao, W.; Zhang, X.; Zheng, X.; Lin, X.; Cao, H.; Zhang, Y.; Sun, Z. Lithium Carbonate Recovery from Cathode Scrap of Spent LithiumIon Battery: A Closed-Loop Process. *Environ. Sci. Technol.* **2017**, *51*, 1662−1669.
(23) Yang, Y.; Zheng, X.; Cao, H.; Zhao, C.; Lin, X.; Ning, P.; Zhang, Y.; Jin, W.; Sun, Z. A Closed-Loop Process for Selective Metal Recovery from Spent Lithium Iron Phosphate Batteries through Mechanochemical Activation. *ACS Sustainable Chem. Eng.* **2017**, *5*, 9972−9980.
(24) Yadav, P.; Jie, C.; Tan, S.; Srinivasan, M. Recycling of cathode from spent lithium iron phosphate batteries. *J. Hazard. Mater.* **2020**, *399*, No. 123068.
(25) Hu, G.; Huang, K.; Du, K.; Peng, Z.; Cao, Y. Efficient recovery and regeneration of $FePO_4$ from lithium extraction slag: Towards sustainable $LiFePO_4$ battery recycling. *Journal of Cleaner Production* **2024**, *434*, No. 140091.
(26) Martín, M. I.; García-Díaz, I.; Lopez, F.A. Properties and perspective of using deep eutectic solvents for hydrometallurgy metal recovery. *Minerals Engineering* **2023**, *203*, No. 108306.
(27) Harper, G.; Sommerville, R.; Kendrick, E.; Driscoll, L.; Slater, P.; Stolkin, R.; Walton, A.; Christensen, P.; Heidrich, O.; Lambert, S.; Abbott, A.; Ryder, K.; Gaines, L.; Anderson, P. Recycling lithium-ion batteries from electric vehicles. *Nature* **2019**, *575*, 75−86.
(28) Mayyas, A.; Steward, D.; Mann, M. The case for recycling: Overview and challenges in the material supply chain for automotive li-ion batteries. *Sustainable Materials and Technologies* **2019**, *19*, e00087.
(29) Jia, K.; Ma, J.; Wang, J.; Liang, Z.; Ji, G.; Piao, Z.; Gao, R.; Zhu, Y.; Zhuang, Z.; Zhou, G.; Cheng, H.-M. Long-Life Regenerated $LiFePO_4$ from Spent Cathode by Elevating the d-Band Center of Fe. *Advanced Materials* **2023**, *35* (5), No. 2208034.
(30) Lander, L.; Cleaver, T.; Rajaeifar, M.; Nguyen-Tien, V.; Elliott, R.; Heidrich, O.; Kendrick, E.; Edge, J.; Offer, G. Financial viability of electric vehicles lithium-ion batteries recycling. *iScience* **2021**, *24* (7), No. 102787.
(31) Gaines, L. Lithium-ion battery recycling processes: Research towards a sustainable course. *Sustainable Materials and Technologies* **2018**, *17*, e00068.
(32) Kwon, O.-s.; Sohn, I. Fundamental thermokinetic study of a sustainable lithium-ion battery pyrometallurgical recycling process. *Resources, Conservation & Recycling* **2020**, *158*, No. 104809.
(33) Fan, Y.; Li, H.; Lu, C.; Chen, S.; Yao, Y.; He, H.; Ma, S.; Peng, Z.; Shao, K. A novel method for recovering valuable metals from spent lithium-ion batteries inspired by the mineral characteristics of natural spodumene. *Journal of Cleaner Production* **2023**, *417*, No. 138043.
(34) Qu, G.; Li, B.; Wei, Y. A novel approach for the recovery and cyclic utilization of valuable metals by co-smelting spent lithium-ion batteries with copper slag. *Chem. Eng. J.* **2023**, *451*, No. 138897.
(35) Asadi Dalini, E; Karimi, G.; Zandevakili, S.; Goodarzi, M. A Review on Environmental, Economic and Hydrometallurgical Processes of Recycling Spent Lithium-ion Batteries. *Mineral Processing and Extractive Metallurgical Review* **2021**, *42*, 451.
(36) Latini, D.; Vaccari, M.; Lagnoni, M.; Orefice, M.; Mathieux, F.; Huisman, J.; Tognotti, L.; Bertei, A. A comprehensive review and classification of unit operations with assessment of outputs quality in lithium-ion battery recycling. *J. Power Sources* **2022**, *546*, No. 231979.
(37) Velázquez-Martínez, O.; Valio, J.; Santasalo-Aarnio, A.; Reuter, M.; Serna-Guerrero, R. A Critical Review of Lithium-Ion Battery

Recycling Processes from a Circular Economy Perspective. *batteries* **2019**, *5* (4), 68.
(38) Sommerfeld, M.; Vonderstein, C.; Dertmann, C.; Klimko, J.; Oráč, D.; Miškufová, A.; Havlík, T.; Friedrich, B. A Combined Pyro- and Hydrometallurgical Approach to Recycle Pyrolyzed Lithium-Ion Battery Black Mass Part 1: Production of Lithium Concentrates in an Electric Arc Furnace. *Metals* **2020**, *10* (8), 1069.
(39) Schirmer, T.; Qiu, H.; Li, H.; Goldmann, D.; Fischlschweiger, M. Li-Distribution in Compounds of the Li_2O-MgO-Al_2O_3-SiO_2-CaO System—A First Survey. *Metals* **2020**, *10* (12), 1633.
(40) Li, H.; Qiu, H.; Schirmer, T.; Goldmann, D.; Fischlschweiger, M. Tailoring Lithium Aluminate Phases Based on Thermodynamics for an Increased Recycling Efficiency of Li-Ion Batteries. *ACS EST Engg* **2022**, *2* (10), 1883−1895.
(41) Wittkowski, A.; Schirmer, T.; Qiu, H.; Goldmann, D.; Fittschen, U. E. A. Speciation of Manganese in a Synthetic Recycling Slag Relevant for Lithium Recycling from Lithium-Ion Batteries. *Metals* **2021**, *11*, 188.
(42) Schnickmann, A.; Hampel, S.; Schirmer, T.; Fittschen, U. E. A. Formation of Lithium-Manganates in a Complex Slag System Consisting of Li_2O-MgO-Al_2O_3-SiO_2-CaO-MnO—A First Survey. *Metals* **2023**, *13*, 2006.
(43) Sundman, B.; Lukas, H.; Fries, S. *Computational thermodynamics: the Calphad method*; Cambridge University Press: Cambridge, 2007.
(44) Saunders, N.; Miodownik, A. P. *CALPHAD (Calculation of Phase Diagrams): A Comprehensive Guide*; Elsevier, 1998.
(45) Van Veldhuizen, D. A.; Lamont, G. B. Evolutionary computation and convergence to a pareto front. In *Late Breaking Papers at the Genetic Programming 1998 Conference*; Stanford University Bookstore, 1998; pp 221−228.
(46) Macleod, B. P.; Parlane, F. G. L.; Rupnow, C. C.; et al. A self-driving laboratory advances the Pareto front for material properties. *Nat. Commun.* **2022**, *13*, 995.
(47) Lu, L.; Anderson-Cook, C. M.; Robinson, T. J. Optimization of design experiments based on multiple criteria ultilizing a pareto frontier. *Technometrics* **2011**, *53* (4), 353−365.
(48) Konar, B.; Van Ende, M.-A.; Jung, I.-H. Critical Evaluation and Thermodynamic Optimization of the Li_2O-Al_2O_3 and Li_2O-MgO-Al_2O_3 Systems. *Metallurgical and Materials Transactions B* **2018**, *49*, 2917.
(49) Konar, B.; Van Ende, M.-A.; Jung, I.-H. Critical evaluation and thermodynamic optimization of the Li-O, and Li_2O-SiO_2 systems. *J. Eur. Ceram. Soc.* **2017**, *37*, 2189−2207.
(50) Konar, B.; Kim, D.-G.; Jung, I.-H. Coupled phase diagram experiments and thermodynamic optimization of the binary Li_2O-MgO and Li_2O-CaO systems and ternary Li_2O-MgO-CaO system. *Ceramics International* **2017**, *43*, 13055−13062.
(51) Li, H.; Ranneberg, M.; Fischlschweiger, M. High-temperature phase behavior of Li_2O-MnO with focus on liquid to solid transition. *JOM-Journal of the Minerals, Metals & Materials Society* **2023**, *75*, 5796.
(52) Eriksson, G.; Pelton, A. D. Critical evaluation and optimization of the thermodynamic properties and phase diagrams of the CaO-Al_2O_3, Al_2O_3-SiO_2, and CaO-Al_2O_3-SiO_2 systems. *Metallurgical Transactions B* **1993**, *24* (5), 807−816.
(53) Chatterjee, S.; Jung, I.-H. Critical evaluation and thermodynamic modeling of the Al-Mn-O(Al_2O_3-MnO-Mn_2O_3) system. *J. Eur. Ceram. Soc.* **2014**, *34*, 1611−1621.
(54) Eriksson, G.; Wu, P.; Blander, M.; Pelton, A. D. Critical Evaluation and Optimization of the Thermodynamic Properties and Phase Diagrams of the MnO−SiO_2 and CaO−SiO_2 Systems. *Canadian Metallurgical Quarterly* **1994**, *33* (1), 13−21.
(55) Wu, P.; Eriksson, G.; Pelton, A. D. Critical Evaluation and Optimization of the Thermodynamic Properties and Phase Diagrams of the CaO-FeO, CaO-MgO, CaO-MnO, FeO-MgO, FeO-MnO and MgO-MnO Systems. *Journal of the American Ceramic Society* **1993**, *76*, 2065−2075.
(56) Konar, B.; Jung, I-Ho. A coupled phase diagram experimental study and thermodynamic optimization of the Li_2O-CaO-Al_2O_3 and Li_2O-CaO-SiO_2 systems, and prediction of the phase diagrams of the Li_2O-CaO-Al_2O3-SiO_2 system. *J. Eur. Ceram. Soc.* **2020**, *40* (5), 2185−2199.
(57) Konar, B.; Kim, D.-G.; Jung, I.-H. Critical thermodynamic optimization of the Li_2O-Al_2O_3-SiO_2 system and its application for the thermodynamic analysis of the glass-ceramics. *J. Eur. Ceram. Soc.* **2018**, *38*, 3881−3904.
(58) Jung, I.-H.; Kang, Y.-B.; Decterov, S. A.; Pelton, A. D. Thermodynamic Evaluation and Optimization of the MnO-Al_2O_3 and MnO-Al_2O_3-SiO_2 Systems and Applications to Inclusion Engineering. Journal of. *Metallurgical and Materials Transactions B* **2004**, *35B*, 259−268.
(59) Kang, Y.-B.; Jung, I. -H; Decterov, S. A.; Pelton, A. D.; Lee, H. -G Critical Thermodynamic Evaluation and Optimization of the CaO-MnO-SiO_2 and CaO-MnO-Al_2O_3 Systems. *ISIJ. International* **2004**, *44*, 965−974.
(60) Pelton, A. D.; Degterov, S. A.; Eriksson, G.; Robelin, C.; Dessureault, Y. The modified quasichemical model I—Binary solutions. *Metallurgical and Materials Transactions B* **2000**, *31* (4), 651−659.
(61) Pelton, A. D.; Chartrand, P. The modified quasi-chemical model: Part II. Multicomponent solutions. *Metallurgical and Materials Transactions A* **2001**, *32* (6), 1355−1360.
(62) Pelton, A. D. A general "geometric" thermodynamic model for multicomponent solutions. *Calphad* **2001**, *25* (2), 319−328.
(63) Barry, T. I.; Dinsdale, A. T.; Gisby, J. A.; Hallstedt, B.; Hillert, M.; Jansson, B.; Jonsson, S.; Sundman, B.; Taylor, J. R. The compound energy model for ionic solutions with applications to solid oxides. *Journal of Phase Equilibria* **1992**, *13* (5), 459.
(64) Bale, C. W.; et al. FactSage thermochemical software and databases, 2010-2016. *Calphad* **2016**, *54*, 35−53.
(65) Chartrand, P.; Pelton, A. D. Modeling the charge compensation effect in silica-rich Na_2O-K_2O-Al_2O_3-SiO_2 melts. *Calphad* **1999**, *23* (2), 219−230.
(66) Ranneberg, M.; Lucas, H.; Li, H.; Graupner, T.; Fischlschweiger, M.; Friedrich, B. Evaluation of Li and Mn influence on Al-Ca-Si-O slag system regarding pyrometallurgical LIB treatment. In *Proceedings of the 8th International Slag Valorisation Symposium*, Mechelen, Belgium; 2023; pp 205−209.
(67) De Jongh, W. K. X-ray fluorescence analysis applying theoretcial matrix correction. Stainless steel. *X-Ray spectrometry* **1973**, *2*, 151−158.
(68) Doebelin, N.; Kleeberg, R. Profex: a graphical user interface for the Rietveld refinement program BGMN. *J. Appl. Crystallogr.* **2015**, *48*, 1573−1580.
(69) Pillars, W.W.; Peacor, D. R. The crystal structure of beta eucryptite as a function of temperature1. *American Mineralogist* **1973**, *58*, 681−690.
(70) Marezio, M. The crystal structure and anomalous dispersion of γ-$LiAlO_2$. *Acta Crystallographica* **1965**, *19*, 396−400.
(71) Lager, G. A.; Meagher, E. P. High-temperature structural study of six olivines. *American Mineralogist* **1978**, *63*, 365−377.
(72) Politaev, V. V.; Petrenko, A. A.; Nalbandyan, V. B.; Medvedev, B. S.; Shvetsova, E. S. Crystal structure, phase relations and electrochemical properties of monoclinic Li_2MnSiO_4. *Journal of Solid State Chemistry* **2007**, *180*, 1045−1050.
(73) Famery, R.; Herpin, P.; Queyroux, F.; Gilles, J. C. Etude structural de la forme ordonnee $LiAl_5O_8$. *Journal of solid state Chemistry* **1979**, *30*, 257−26.
(74) Rosciano, F.; Pescarmona, P. P.; Houthoofd, K.; Persoons, A.; Bottke, P.; Wilkening, M. Torwards a lattice-matching solid-state battery: synthesis of a new class of lithium-ion conductors with the spinel structure. *Physical Chemistry Chemical Physics* **2013**, *15*, 6107−6112.
(75) Wende, C. *Synthese und Charakterisierung von Spinellen im quasiternären System "$LiO_{0.5}$ - MnO_x - FeO_x"*, Dissertation, Technische Universität Dresden, 2006, 164 S.

https://doi.org/10.1021/acssusresmgt.4c00064
ACS Sustainable Resour. Manage. 2024, 1, 1170−1184

(76) Swainson, I. P.; Dove, M. T.; Schmahl, W. W.; Putnis, A. Neutron Diffraction Study of the Akermanite-Gehlenite Solid Solution Series. *Physics and Chemistry of Minerals* **1992**, *19*, 185−195.
(77) Lehmann, H.; Hesselbarth, H. Zur Kenntnis der Lithiumaluminate. 1. Über eine neue Modifikation des $LiAlO_2$. *Zeitschrift für anorganische und allgemeine Chemie* **1961**, *313* (1-2), 117−120.
(78) Tabero, P.; Frackowiak, A.; Dabrowska, G. Reinvestigation of the Li_2O-Al_2O_3 system. *Part I: $LiAlO_2$and Li_3AlO_3* **2021**, *23* (3), 30−36.

https://doi.org/10.1021/acssusresmgt.4c00064
ACS Sustainable Resour. Manage. 2024, 1, 1170−1184